Chapter 3

High-Q Photonic Crystal Microcavities in InAsP/InGaAsP Multi-Quantum-Well Membranes

3.1 Introduction

With the high-Q photonic crystal microcavity designs of chapter 2 in hand, the next step is the experimental demonstration of these devices. There have typically been two experimental techniques that have been used to characterize PC microcavities. The first involves fabrication of the devices within an active (light-emitting) material, where the properties of the cavity modes are studied by optical pumping and examination of the characteristics of the resulting emission. This method has been used in a number of studies, including refs. [8, 12, 42]. Alternately, other authors [49] have chosen to fabricate the cavities within a passive (non-light-emitting) material, and have probed them by using accompanying microfabricated waveguides to couple light into and out of the cavities. In chapter 4, we will discuss the relative merits of these two approaches. For now, we will focus on our efforts on the first technique, where we have fabricated cavities in a InP-based multi-quantum-well (MQW) membrane and studied their emission characteristics. The results presented in this chapter are largely based on refs. [43] and [44]. The former paper details the primary results of our measurements, including the demonstration of $Q \sim 1.3\times10^4$ in a PC microcavity, which represented an improvement by almost a factor of 5 over what had been demonstrated to that point ($Q \sim$2,800 in ref. [12]).[1] The second paper is a detailed description of the fabrication processes developed to create these InP-based structures, and in particular, highlights the advances in plasma etching that

[1] $Q \sim$4,000 had also been demonstrated in a PC cavity, albeit a larger mode volume design where the defect consisted of several missing air holes [112].

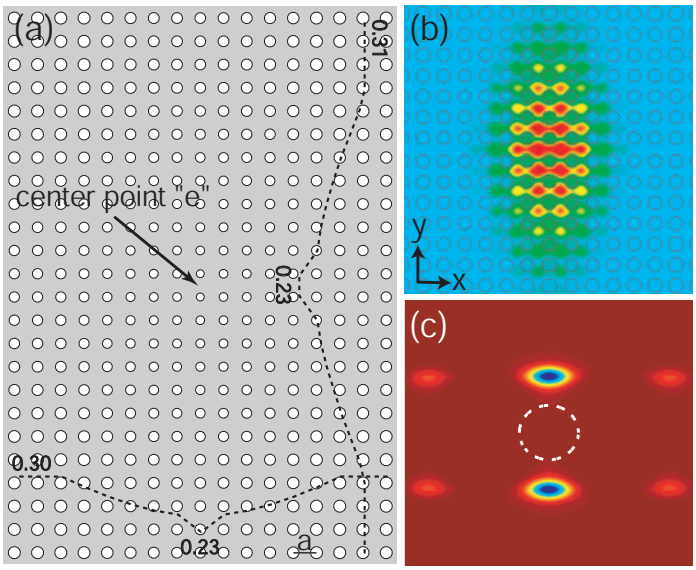

Figure 3.1: (a) Graded square lattice cavity designed in ref. [21]; dotted lines show the grade in hole radius (r/a) along the central $\hat{x}$ and $\hat{y}$ axes of the cavity. For the A_2 mode ($a/\lambda_o = 0.25$): (b) Magnetic field amplitude (H_z) in the center of the PC membrane, and (c) Fourier transformed dominant electric field component (E_x). The dashed circle in (c) denotes the cladding light cone, showing that vertical radiation has been significantly suppressed.

have made the creation of high quality semiconductor microphotonic structures possible.

In chapter 2, high-Q PC cavities were designed by considering the Fourier space properties and symmetry of cavity modes. An important feature of these designs is their robustness, in that perturbations to the size and shape of *individual* holes do not deteriorate the Q significantly. Vertical radiation losses, which are characterized by the presence of power at in-plane momentum components ($\mathbf{k}_\perp$) that lie within the light cone of the slab waveguide cladding, are reduced by choosing modes of a specific symmetry. In particular, the modes selected are those that are odd about mirror planes normal to the direction of the mode's dominant Fourier components. For the square lattice cavities studied in chapter 2, one such mode is a donor-type mode (labeled A_2 due to its symmetry) centered in the dielectric between two rows of air holes (point *e* in fig. 3.1). Further improvements to both the in-plane and vertical loss are achieved by grading the lattice as shown in fig. 3.1(a). Figure 3.1(b)-(c) shows the magnetic field amplitude and Fourier transformed dominant electric field component for the resulting A_2 mode as calculated by finite-difference time-domain (FDTD) simulations. FDTD calculations predict $Q \sim 10^5$ for this mode, with a modal volume $V_{\text{eff}} \sim 1.2(\lambda/n)^3$. Calculations show that the grade used in fig. 3.1(a) can be varied fairly significantly without degrading the Q to a value less than $\sim 2\text{x}10^4$.

Table 3.1: Epitaxy for 1.3 μm PC microcavity lasers. 1.12Q stands for quaternary GaInAsP layers, lattice matched to InP, with photoluminescence peak at 1.12 μm ($Ga_{0.15}In_{0.85}As_{0.32}P_{0.68}$). The quantum well layers are $InAs_{0.48}P_{0.52}$ and the barrier layers are $Ga_{0.24}In_{0.76}As_{0.32}P_{0.68}$. Total membrane thickness after undercutting the sacrificial InP layer is 252 nm.

Layer	Materials	Strain (rel. to InP)	Thickness	Doping (cm^{-3})
Separate confinement	1.12Q	unstrained	810 Å	undoped
Half-barrier	GaInAsP	0.65% tens.	60 Å	undoped
Active region	5 wells	1.5% comp.	60 Å	undoped
	4 barriers	0.65% tens.	120 Å	undoped
Half-barrier	GaInAsP	0.65% tens.	60 Å	undoped
Separate confinement	1.12Q	unstrained	810 Å	undoped
Sacrificial buffer layer	InP	unstrained	15000 Å	undoped
Etch stop	InGaAs	unstrained	200 Å	undoped
Substrate	InP	unstrained	N/A	N/A

3.2 Fabrication of PC cavities in InP-based multi-quantum-well membranes

To measure the properties of the donor-type A_2 mode, graded square lattice PC cavities were fabricated in an active material that was grown by Dr. Jianxin Chen at Bell Laboratories through solid-source molecular beam epitaxy, as described elsewhere [113]. It consists of five InAsP compressively-strained quantum wells separated by InGaAsP barriers, as shown in table 3.1. The peak emission wavelength is at λ=1284 nm, and the epitaxy is designed so that, upon undercut of the 1.5μm sacrificial InP layer, a 252 nm thick free-standing membrane will be formed (the thickness is chosen to be consistent with the emission wavelength of the quantum wells and the FDTD-calculated frequency of the cavity mode). The creation of the 2D PC membrane is accomplished through electron beam lithography, pattern transfer to a SiO_2 mask using an inductively coupled plasma reactive ion etch (ICP/RIE), and a high-temperature (205 ^oC) Ar-Cl_2 ICP/RIE etch through the active material into a sacrificial InP layer. The sample is undercut by removing the InP layer with a HCl:H_2O (4:1) solution. These fabrication steps are described in detail in the following sections. In addition, appendix C reviews some general considerations in the fabrication of microphotonic structures.

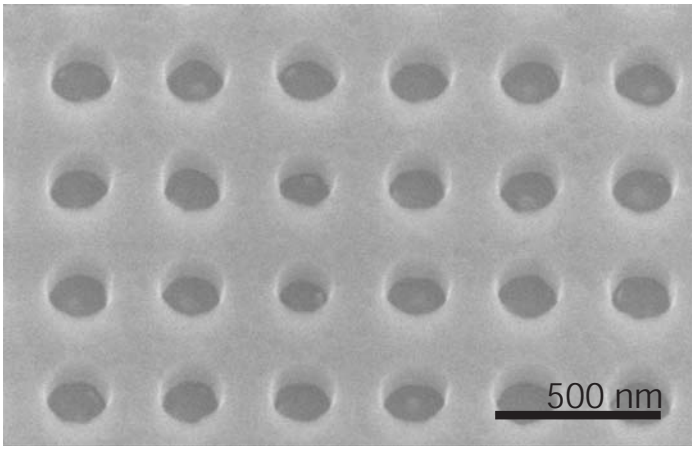

Figure 3.2: Angled view SEM image of the SiO_2 etch mask

3.2.1 Mask creation

A 200 nm thick SiO_2 mask layer is deposited on the epitaxial wafer by an Oxford Instruments Plasma Technology (OIPT) Plasmalab 100 plasma-enhanced chemical vapor deposition (PECVD) tool. The PC patterns are created through electron beam (e-beam) lithography of an $\sim$ 350 nm thick layer of resist, typically Zeon Chemical's ZEP-520A. Each cavity consisted of a total of 32 rows and 25 columns of air holes, with a lattice spacing of $a = 305$, 315, 325, or 335 nm (normalized frequency of $a/\lambda \sim 0.25$ at $\lambda \sim 1.3$ μm), for total cavity dimensions on the order of 8x11μm. The designed grade produces holes with radii between $r =$ 70-110 nm.

To etch the SiO_2 mask layer, an OIPT Plasmalab 100 ICP/RIE tool with a C_4F_8 gas chemistry was used. The requirements of the process were that the etched sidewalls be as smooth and vertical in slope as possible. Due to the relatively poor dry etch resistance of the e-beam resist, a third requirement was to create a sufficiently low power etch to avoid excessive damage to the resist, so that the desired shape and size of the holes remained intact. Along with this, the low etch selectivity of the resist ($\sim$1:1) placed an upper limit on the thickness of the oxide layer used.

The etch profile and sidewall roughness were examined as a function of ICP power (400-600 W), RF power (50-100 W), and C_4F_8:O_2 gas chemistry (between 20:0 sccm and 15:5 sccm), keeping a fixed chamber pressure (P_{ch}=6 mTorr), lower electrode temperature ($\sim 20\,^{\circ}$C), and He backside cooling (20 Torr, $\sim$ 20 sccm). To maintain the integrity of the ICP/RIE chamber, O_2 plasma cleans were periodically run between etches. For the process conditions examined, we did not observe significant changes in the sidewall roughness. For a given set of RF and ICP powers, we saw an increase in the sidewall verticality with increased C_4F_8 content, without any polymerization, so that a pure C_4F_8 gas chemistry was finally chosen. The RF and ICP powers were then adjusted to reduce

damage to the resist as much as possible without causing degradation of the sidewall profile. For the final process conditions chosen (RF = 80 W, ICP = 600 W, 20 sccm C_4F_8), an etch time of ~ 2 minutes etched through the oxide layer completely and produced a sidewall angle of $\sim 85^\circ$ as estimated through cross sectional SEM images. A scanning electron microscope (SEM) image of the etched SiO_2 mask layer is shown in fig. 3.2, where an O_2 plasma has been used to remove the remnants of the resist.

3.2.2 InAsP/InGaAsP membrane etch and undercut

The next step is an ICP/RIE etch through the InAsP/InGaAsP membrane layer into the InP sacrificial layer. From the standpoint of cavity Q, it is of critical importance that the etched sidewalls be both smooth and vertical, as sidewall roughness will produce scattering loss and an angled sidewall will break the vertical symmetry of the slab and causes radiative coupling to modes of the opposite symmetry (TM-like modes, for which there is no in-plane bandgap) [114]. As we shall discuss, the requirements on the ICP/RIE etch are also influenced by the ensuing undercut wet etch, as the necessity to undercut all of the holes in the lattice places a lower limit on the etch depth into the InP layer.

Dry etching of In-containing III-V semiconductors is typically accomplished using one of two gas chemistries [115]. The first, a CH_4/H_2 chemistry, is done at room temperature and can produce smooth etched morphologies, but with the drawbacks of a relatively slow etch rate ($\lesssim 60$ nm/min) and heavy polymer deposition during the process. Cl_2-based plasmas have also been used, but the low volatility of $InCl_x$ products at room temperature necessitate some form of heating during the etch. This has been done in the past using a high-density ICP-produced Cl_2 plasma by Fujiwara et al. [116], where the production of smooth etched surfaces is most likely due to a combination of the plasma providing local surface heating of the sample and an increased efficiency in the sputter desorption of the $InCl_x$ products [115]. Alternately, a number of studies have successfully used a heated wafer table ($\gtrsim 150\,^\circ$C) with an Ar-Cl_2 chemistry to achieve a volatility of the $InCl_x$ products sufficient to etch InP-related compounds with vertical sidewalls and smooth surface morphologies. In a recent study [117], Rommel and his collaborators optimize this etch (using H_2 to control the sidewall profile) in an ICP/RIE system to produce sub-micron width racetrack resonators with a Q of $8,000$. We adopt an etch similar to the process used in that work. An important difference between this work and much of the published work on InP etching is the geometry we are etching, as the small features (~ 150 nm diameter holes) likely inhibit both the flow of ionized source gases

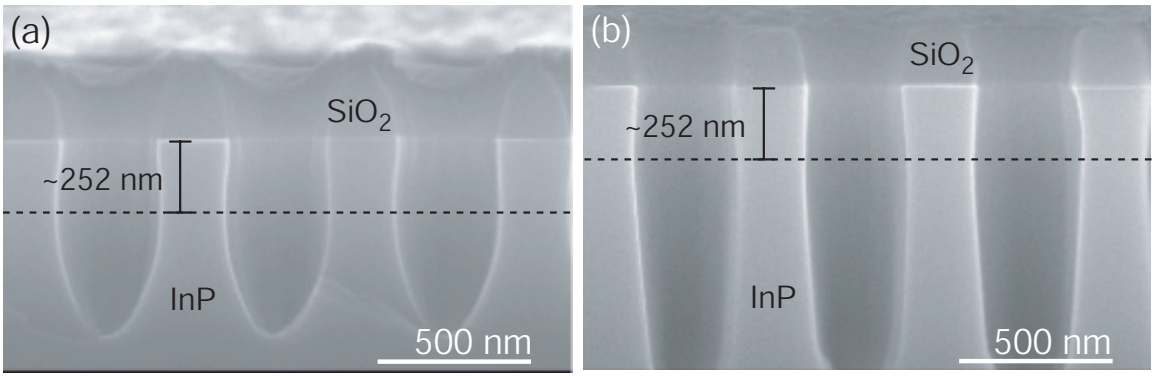

Figure 3.3: SEM cross sectional images of the InP etch for increasing wafer table temperature (a) T=150 °C, t_{etch}=120 s, etch depth = 650 nm, and (b) T=180 °C, t_{etch}=165 s, etch depth = 1 μm. For these etches, RF=100 W, ICP=300 W, P_{ch} = 2 mTorr, Ar:Cl_2=12:3 sccm. The top 252 nm, highlighted in each SEM image, corresponds to the active waveguiding layer thickness (final membrane thickness) in the actual InAsP/InGaAsP laser material used in the device fabrication.

to the etching surfaces as well as the removal of etched by-products. This will affect both the etch rates we observe (often a factor of two or more lower than the etch rates in open areas) and the resulting surface morphology.

We examined etched samples (initially etching pure InP rather than the InAsP/InGaAsP QW material) primarily as a function of gas composition (Ar:Cl_2 ratio between 9:6 sccm and 13:2 sccm), stage temperature (20-225 °C), RF power (100-200 W), and ICP power (250-400 W). It quickly became apparent that elevated temperatures were indeed necessary, as the InP did not etch cleanly at room temperature. A preliminary etch with a stage temperature of 150 °C and an Ar:Cl_2 ratio of 12:3 sccm is shown in fig. 3.3(a). By further increasing the stage temperature (fig. 3.3(b)), the profile of the holes becomes more vertical and the total etch rate increases. We chose a stage temperature of 205 °C as temperatures above this value provided no added benefit to the sidewall smoothness and profile of the etched holes. With a stage temperature of 205°C, the Ar:Cl_2 gas ratio was varied around 12:3 sccm. It was found that higher concentrations of Cl_2 produce a slight amount of sidewall roughness, while lower concentrations produce a more pronounced overcut etch profile. With a stage temperature of 205°C and an Ar:Cl_2 gas ratio of 12:3 sccm, the ICP and RF powers were then varied about values of 300 W and 100 W, respectively. Larger RF powers caused deterioration of the oxide mask, producing some sidewall erosion, while smaller RF powers reduced the etch anisotropy. We noticed little variation in etch quality as a function of ICP power over the range of ICP powers explored. The final InGaAsP material etch conditions that we settled

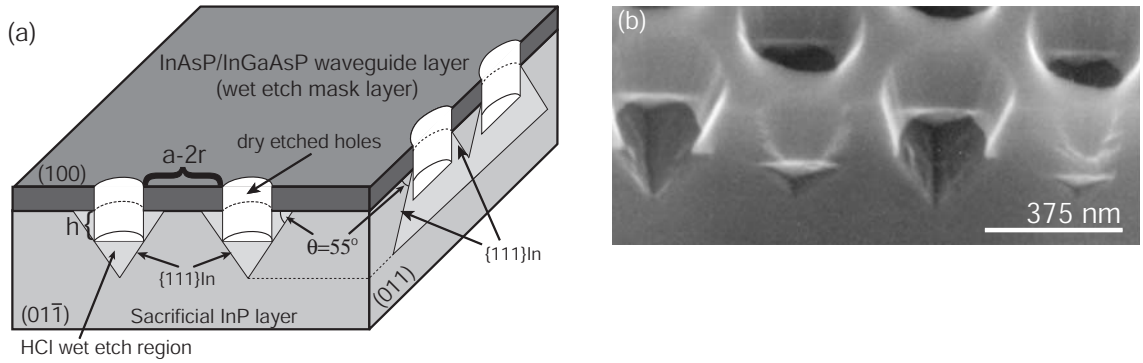

Figure 3.4: (a) Illustration of the shape of the etched surfaces resulting from the crystallographic nature of the InP wet etch (h = etch depth below waveguiding layer into InP sacrificial layer, r = hole radius, a = lattice spacing, $(a-2r)$ = gap between holes). (b) SEM image of a partially undercut membrane (where the membrane layer was etched with a CAIBE system) showing the $\{111\}_{\text{In}}$ crystal plane facets. Both figures adapted from previous work [3].

on were: T=205 °C, Ar:Cl_2=12:3 sccm, P_{ch}=2 mTorr, RF=100 W, and ICP=300 W. With these process conditions and an etch time of 120 seconds, an etch depth of 1.5 μm was achieved, with a selectivity of $\sim$ 20:1 to the oxide mask.

To remove the sacrificial InP layer and undercut the membrane, an HCl:H_2O (4:1) solution was used. HCl etches the InP layer at a much faster rate than it does the active waveguide layer (composed of lower Phosphorous (P) percentage alloys of InAsP and InGaAsP compounds), providing the necessary degree of etch selectivity [118]. The resolution and selectivity of the etch are improved by cooling the solution in an ice-water bath to $\sim 4^{\circ}$C, thereby reducing the material etch rates, and in particular, the total amount of waveguide material that is necessarily etched. The typical time to fully undercut the membrane was $\sim$ 12 minutes (depending on the lattice spacing and hole size of the PC pattern). To protect the top sample surface, the remnants of the oxide mask layer were removed only after the undercut etch was performed.

The HCl:H_2O solution etches InP with a strong crystallographic dependence [119]. The resulting etch shape is determined by the differences in etch rate of different crystallographic planes as well as boundary conditions imposed by masking layers (which limit the available etch angles). The etch shape will ultimately converge to one determined by the slowest set of etch planes, which are the Indium (In) rich $\{111\}$ planes ($\{111\}_{\text{In}}$) for the InGaAsP material system. For a (100) InP wafer, the $\{111\}_{\text{In}}$ planes are at an angle of $\sim 55^{\circ}$ from the surface normal as shown in fig. 3.4(a). For concave mask openings, this results in an etch cross section which is an overcut V-shape in the $(01\bar{1})$ plane and an undercut overhanging shape in the (011) plane. This is shown schematically

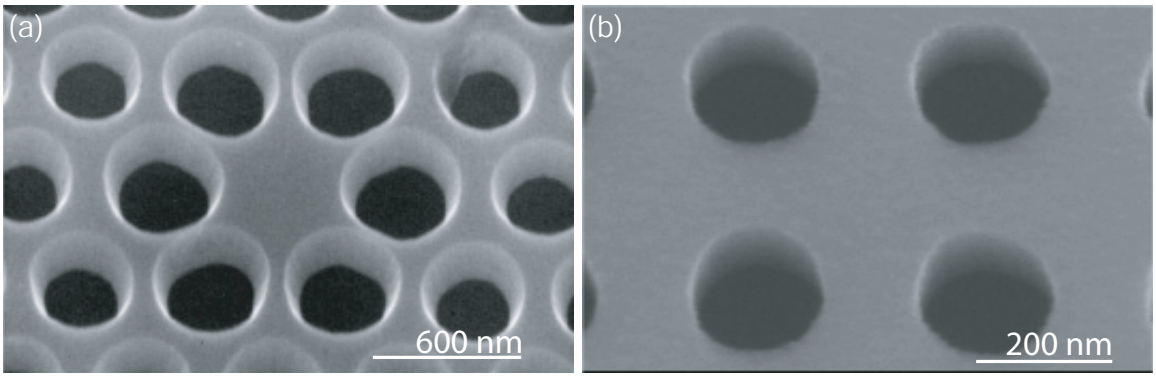

Figure 3.5: SEM micrographs of fully fabricated devices: (a) previous work using CAIBE for the membrane etch [3], and (b) the current work, using ICP/RIE for the membrane etch.

in fig. 3.4(a), and can also be seen clearly in the partially undercut holes of fig. 3.4(b). As in fig. 3.4(b), once the etch has proceeded to the $\{111\}_{\mathrm{In}}$ planes, unless there is an overlap between the $\{111\}_{\mathrm{In}}$ planes of adjacent holes, the etch will grind to a halt and the waveguiding layer will not completely undercut (longer etch times and/or higher temperatures may be employed to further undercut the structure, however, selectivity to the active waveguiding layer will have been lost). As a result, the ICP/RIE dry etch depth into the underlying sacrificial InP layer sets a lower limit on the radius (r) and lattice spacing (a) of holes that can be undercut. More precisely, using the nomenclature of fig. 3.4(a), the adjacent $\{111\}_{\mathrm{In}}$ planes in the $(01\bar{1})$ plane overlap for $h \geqslant (a/2 - r)\tan(55^\circ)$, so that h increases as r decreases for a given a. This was a limitation of previous work done using an Ar:Cl_2 chemically assisted ion-beam etch (CAIBE) [3], where total etch depths were typically ~ 340 nm, corresponding to $h \sim 130$ nm. For the fabricated lattice spacings in that work, $a = 500$ nm, this produces a minimum possible undercut hole radius of $r/a = 0.32$. The ability to undercut smaller holes (preferably as small as $r/a = 0.20$) is of critical importance to the cavity Q, as holes that are too large in size will significantly raise the frequency of a given mode and hence the size of the cladding light cone, thereby increasing the amount of power radiating vertically [21]. Our etch depth of ~ 1.5 μm ($h \sim 1.25$ μm) is not only deep enough to ensure that the $\{111\}_{\mathrm{In}}$ crystal planes overlap for even the smallest desired holes ($r/a = 0.23$), but also aids the undercut process by reducing the total amount of material that needs to be removed.

Figure 3.5 compares the results of previous fabrication methods [3] with the current work. Both images show smooth membrane sidewalls, but the sidewall profile is considerably more sloped in the former work (this is also evident in fig. 3.4(b)). The higher degree of verticality and the ability

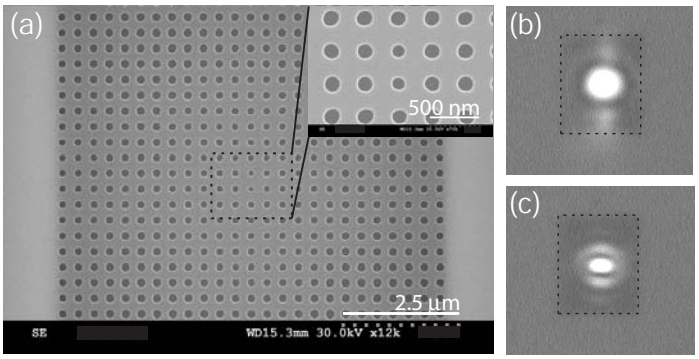

Figure 3.6: (a) SEM image of a graded lattice PC microcavity in the InAsP multi-quantum-well material. Lattice constant $a \sim 305$ nm, membrane thickness $d = 252$ nm. Optical image of cavity pumped with a (b) diffuse beam and (c) focused beam (dashed rectangle represents the physical extents of the undercut PC).

to undercut the smallest desired holes ($r/a = 0.23$) are the primary advantages of the present work. Although optimization of all of the masking steps was necessary to achieve this result, the ICP/RIE membrane etch is the critically important step that creates these advantages.

3.3 Photoluminescence measurements

Using the fabrication techniques described in the previous section, we created arrays of PC cavities within the InP-based MQW epitaxy. Devices are optically pumped (10 ns pulse width, 300 ns period) at room temperature with a semiconductor laser at 830 nm through a 20X objective lens, also used to collect emitted photoluminescence (PL) into an optical spectrum analyzer (OSA). A schematic of the setup that was used is shown in fig. 3.7. We initially pump the cavities with a broad pump beam (see fig. 3.6(b), area $\sim 21\mu\text{m}^2$) for two reasons: (i) the broad pump beam covers a significant portion of the cavity area, so that after diffusion of carriers, the majority of the cavity should be pumped and therefore non-absorbing, and (ii) use of a broad pump beam limits the effects of thermal broadening, which, as discussed below, are significant for focused pump beams.

A typical L-L (light-in versus light-out) curve using the broad pump beam condition is shown in fig. 3.8(a) for a device with $a = 335$ nm, where the power in the laser line is taken over a 10 nm bandwidth about the laser wavelength of $\lambda = 1298.5$ nm. In addition, the off-resonance background emission at $\lambda = 1310$ nm was measured over a similar 10 nm bandwidth. For low pump powers ($<$ 300 μW), the off-resonance emission and resonant wavelength emission linearly increase with pump power and are essentially identical in level, i.e., no resonance feature is observed. Above 300 μW, we begin to see a resonance peak in the spectrum and a characteristic super-linear transition from below threshold to above threshold follows. To estimate the position of threshold we extrapolate

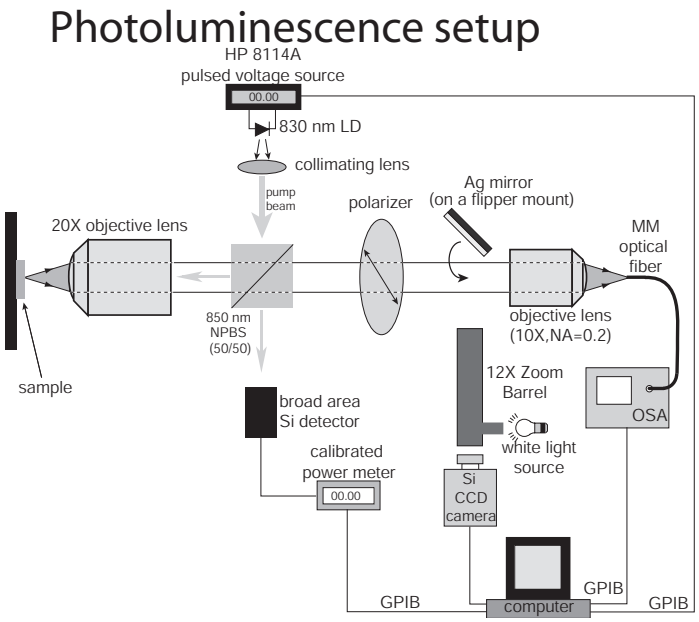

Figure 3.7: Schematic of the photoluminescence measurement setup. Acronyms used in this diagram: NPBS: non-polarizing beamsplitter, LD: laser diode, MM: multimode, OSA: optical spectrum analyzer

back the L-L curve from above threshold (fig. 3.8(b)), giving an approximate threshold pump level of 360 μW. A plot of the off-resonance emission (fig. 3.8(c)) shows a (weak) slope change around 365 μW giving a similar estimate for the threshold value. The kink in the off-resonance background emission L-L curve can be attributed to the clamping of the carrier density (gain) in the region of the cavity mode and consequent saturation of the off-resonance (non-lasing modes') emission. The background emission continues to increase after crossing threshold (rather than completely saturating) as a result of the pumping of areas which are outside of the cavity mode volume and thus not affected by the gain clamping (non-equilibrium carrier distributions [120] may also play a role).

In order to estimate the cold cavity Q value of the PC microcavity mode we measured the linewidth of the resonance in the PL around threshold. The full-width half-maximum (FWHM) linewidth narrows from 0.138 nm (at the lowest pump level we could accurately measure the linewidth, 320 μW) down to 0.097 nm at threshold. A simple steady state rate equation model [121] of the cavity photon and excited state populations estimates the threshold pump level (with this beam size) to be ~ 350 μW for $Q \sim 10^4$ in this quantum well active material, close to the experimentally measured value. In this model the transparency carrier density occurs within 10% of the threshold carrier density for cavity modes with $Q > 10^4$. A PL spectrum (fig. 3.8(a), inset) for this device with the broad pump conditions, measured soon after detection of a resonance feature in the spectrum and below the estimated threshold level by about 10%, shows a resonance linewidth $\Delta\lambda = 0.100$ nm, corresponding to a best estimate of the cold cavity $Q \sim 1.3\text{x}10^4$. Above threshold

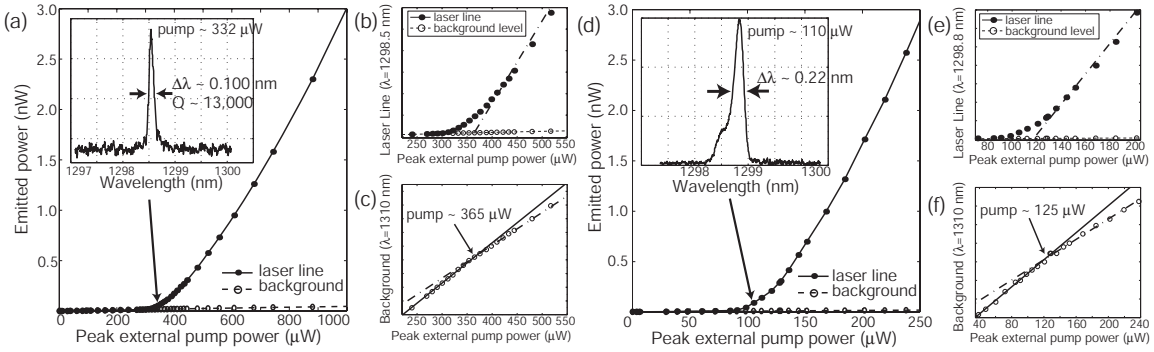

Figure 3.8: (a) L-L curve and subthreshold spectrum (inset) of a graded square lattice PC microcavity pumped with a spatially broad pump beam (10 ns pulse, 300 ns period), and zoomed-in plots of (b) laser threshold and (c) background emission for the same diffuse pump beam. (d) L-L curve and subthreshold spectrum (inset) taken with a focused pump beam spot, showing increased thermal broadening in comparison to the diffuse pump beam spectrum, and zoomed-in plots of (e) laser threshold and (f) background emission. The "guide" lines displayed in (b), (c), (e), and (f) are least-squares fits of the data taken over several points above and below the lasing transition region.

we do not see further linewidth narrowing due to the resolution limit of our scanning monochromator (0.08 nm); thermal broadening of the emission line during the pump pulse and incomplete saturation of the carrier density [120] may also play a role.

By using a more tightly focused beam (see fig. 3.6(c), area $\sim 8\ \mu m^2$), the lasing threshold is considerably reduced. In fig. 3.8(d)-(f), we plot the L-L curve for the laser line and off-resonance background emission using such a pump beam. The plots are qualitatively similar to those for the diffuse pump beam; we begin to see a resonance feature when the pump power exceeds 95 μW. Estimates for the threshold pump power from the laser line curve and off-resonance background emission are 120 μW and 125 μW, respectively. Through further optimization of the pump beam, lasers with thresholds as low as $\sim 100\ \mu$W have been observed. From the subthreshold spectrum shown in the inset of fig. 3.8(d) it is readily apparent that the lineshape has thermally broadened (the measured linewidth is now 0.220 nm), as evidenced by its asymmetric shape on the short wavelength side. To reduce the effects of this thermal broadening, the duty cycle can be decreased to 1% (1 μs period and 10 ns pulse width), resulting in a less asymmetric resonance and subthreshold linewidth of approximately 0.13 nm. Conversely, we have also increased the duty cycle to 25% (1 μs period and 250 ns pulse width) and still observe lasing; heating in the membrane precludes lasing at even higher duty cycles.

To determine whether the laser mode described above is indeed the localized A_2 mode of fig. 3.1,

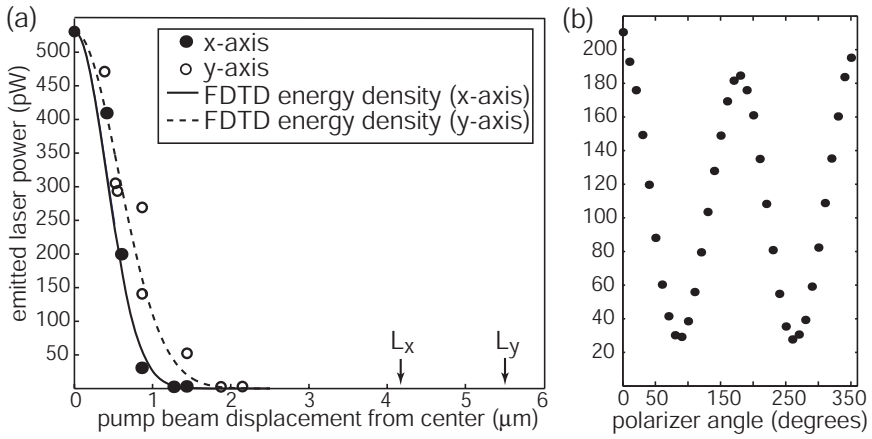

Figure 3.9: (a) Emitted laser power as a function of pump position along the $\hat{x}$ and $\hat{y}$ axes of the cavity. FDTD-generated Gaussian fits to the *envelope* of the electric field energy density of the cavity mode are shown for comparison (note that the effective mode volume is calculated from the *peak* electric field energy density). L_x and L_y correspond to the physical extent of the PC in the $\hat{x}$- and $\hat{y}$-direction, respectively. (b) Emitted laser power as a function of polarizer angle with respect to the $\hat{x}$ axis of the cavity.

we have measured polarized intensity in the far-field as well as the sensitivity of the emitted laser power to pump position. The measurements show the mode to be predominantly polarized along the $\hat{x}$-axis (fig. 3.9(b)) of the cavity, consistent with FDTD results, and eliminating the possibility that the mode is of the other potential symmetry supported by the cavity (B_2, as discussed in chapters 1 and 2). Furthermore, the lasing mode discussed above is the longest wavelength mode observed in the devices tested (higher frequency resonances are observed in some detuned devices), suggesting that it is the fundamental mode shown in fig. 3.1(b), and not a higher order version of it. In fig. 3.9(a) we show measurements of the emitted laser power as a function of the pump beam position (taken to be the center of the beam) relative to the center of the cavity (uncertainty in the pump position is ~ 0.25 μm). The measurements indicate the mode is highly localized within the center of the cavity, consistent with simulations.

3.4 Summary

In summary, this chapter reports on the observation of linewidths of $\Delta\lambda = 0.10$ nm, corresponding to a cavity Q of 1.3x10^4, in subthreshold measurements of graded square lattice photonic crystal microcavity lasers fabricated in an InAsP/InGaAsP multi-quantum-well membrane. In addition, lasing is seen at threshold peak external pump powers as low as 100 μW. Measurements of the

emitted power as a function of pump position show the mode to be strongly localized and give an estimate of the modal localization that is consistent with FDTD results. This realization of a high Q, small mode volume microcavity is an important step in demonstrating the potential of PC microcavities for use in optoelectronics and quantum optics.

The Q values that we demonstrated in these PC microcavity lasers were at the time, the highest that had been seen in a PC microcavity, but were quickly exceeded by devices demonstrated by both the group of S. Noda at Kyoto University [51], and by our own group at Caltech, in devices I created in silicon membranes [52], which will be described in detail in the following chapter. To the best of my knowledge, within the InP material system, there has not yet been a demonstration of a PC microcavity with a Q higher than the devices described in this chapter.

More importantly, the measurements we performed on these devices give us some indication of the limitations of these spectrometer-based studies using cavities fabricated in an active material. The most obvious limitation is the resolution of the spectrometer; for the optical spectrum analyzer we used, this was 0.1 nm, but even for instruments with a longer path length, resolutions better than 0.01 nm are difficult to achieve. Of course, other resolving instruments, such as filters based on Fabry-Perot cavities (which can be commercially obtained in both free-space and fiber-based geometries), can be used to achieve much better resolution. That being said, it is still clear that there are other advantages to adopting a measurement technique that did not require an active medium. This would open up PC cavities fabricated in materials such as silicon (which had been shown to have relatively low material loss at telecommunications wavelengths) for investigation, and it would allow for a simple measurement of Q that would not be subject to the influence of material gain. Most importantly, developing a technique to efficiently get light into and out of the PC microcavities would make these devices much more functional and integrable within more sophisticated experiments or systems. In the next chapter, I describe our work with a fiber-based probe that enables such advances.